Determining the Orientation of Ocean-Bottom Seismometers on the Seafloor and Correcting for Polarity Flipping via Polarization Analysis and Waveform Modeling

Gaohua Zhu[1], Hongfeng Yang[*1], Jian Lin[2,3], and Qingyu You[4]

Abstract

The erroneous flipping of polarity in seismic records of ocean-bottom seismometers (OBSs) could go unnoticed and undiagnosed because it is coupled with unknown horizontal orientation of OBS instruments on the seafloor. In this study, we present detailed approaches to first identify potential errors in the flipping polarity of individual OBS instruments, and then determine the correct orientation of OBS instruments on the seafloor. We first conduct a series of tests by artificially flipping the polarity of seismic records of the Global Seismographic Network stations to determine the effects on orientation estimates, utilizing polarization characteristics of teleseismic *P* and Rayleigh waves, respectively. The tests demonstrate that erroneous polarity reversal in seismic recording could cause false estimates and reverse radial (R) and tangential (T) components. We determine the sensor orientations through comparing the observed waveforms to the synthetic waveforms, which could solve the ambiguity of R and T directions caused by potential erroneous polarity reversal of OBS data. We then apply the approaches to an OBS data set collected in the southern Mariana subduction zone to obtain the correct orientation for 9 out of 12 OBS instruments.

Cite this article as Zhu, G., H. Yang, J. Lin, and Q. You (2020). Determining the Orientation of Ocean-Bottom Seismometers on the Seafloor and Correcting for Polarity Flipping via Polarization Analysis and Waveform Modeling, *Seismol. Res. Lett.* **XX**, 1–12, doi: 10.1785/0220190239.

Introduction

Waveform data recorded at ocean-bottom seismometers (OBSs) have significantly advanced our understanding of plate tectonics and the internal structure of the Earth by extending seismic network to the vast Earth surface covered by the ocean. Studies based on travel times of seismic waves, such as earthquake location and seismic tomography, have been pervasively conducted using OBS data at subduction zones in recent decades (Tibi *et al.*, 2008; Emry *et al.*, 2011; Barklage *et al.*, 2015; Cai *et al.*, 2018; Zhu *et al.*, 2019). However, because sensors are settled onto the seafloor through a free-fall process during typical OBS deployments, it is more difficult to utilize OBS waveforms than land data because of time drifting (Le *et al.*, 2018; Zhu *et al.*, 2019), potential tilting (Crawford and Webb, 2000; Hung *et al.*, 2019), and unknown orientations of horizontal components (Stachnik *et al.*, 2012; Scholz *et al.*, 2016). Compared with land seismic data, waveform-based studies using OBS data are limited due to poorly oriented horizontal components and low signal-to-noise ratio (SNR) of OBS data. In addition, unexpected problems with the OBS stations (e.g., randomly flipping waveforms) could result in anomalous observations, making it more complicated to precisely estimate orientation of OBS horizontal components.

Several approaches have been used to determine sensor orientations. For example, analyzing the polarization of the vectorial seismic signals (body wave or Rayleigh wave) from known earthquakes can provide information about the azimuth of sensors (Vidale, 1986; Baker and Stevens, 2004; Stachnik *et al.*, 2012; Rueda and Mezcua, 2015; Scholz *et al.*, 2016). Moreover, a recent study demonstrates that the sensor orientations can be estimated via analyzing the polarization of Rayleigh waves retrieved from ambient-noise cross correlation (Zha *et al.*, 2013; Xu *et al.*, 2018). However, these approaches may yield false results when the original OBS recording suffers erroneous,

1. Earth System Science Programme, The Chinese University of Hong Kong, Shatin, Hong Kong, China; 2. Department of Geology and Geophysics, Woods Hole Oceanographic Institution, Woods Hole, Massachusetts, U.S.A.; 3. Key Laboratory of Ocean and Marginal Sea Geology, South China Sea Institute of Oceanology, Chinese Academy of Sciences, Guangzhou, China; 4. Key Laboratory of Petroleum Resources Research, Institute of Geology and Geophysics, Chinese Academy of Sciences, Beijing, China

*Corresponding author: hyang@cuhk.edu.hk

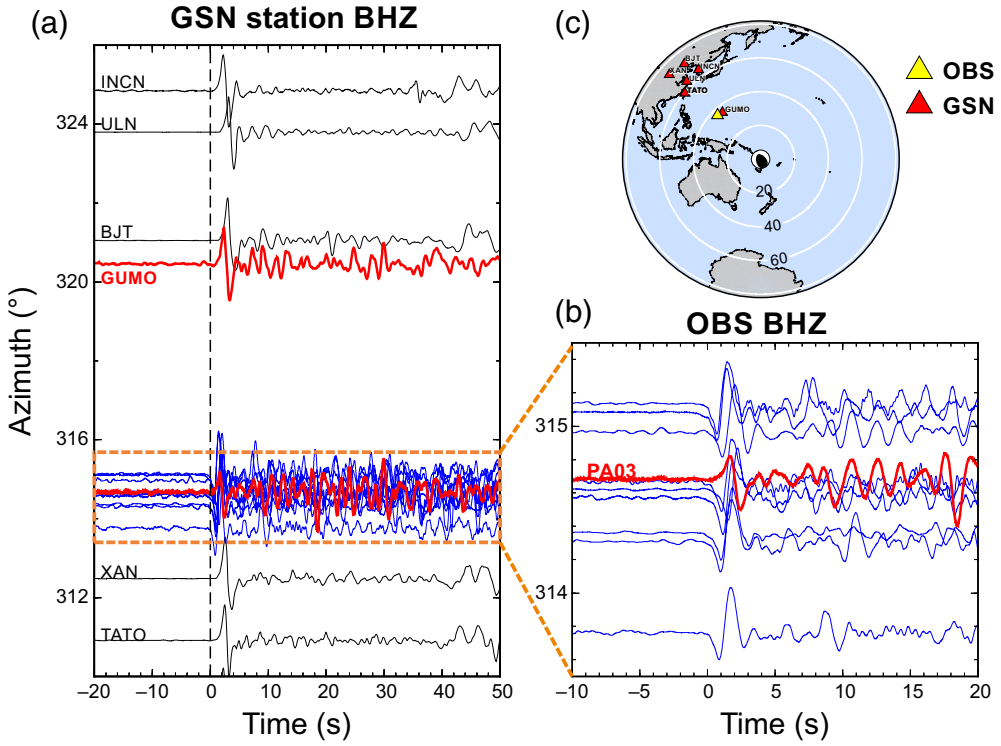

Figure 1. The polarity reversal of ocean-bottom seismometer (OBS) vertical components identified from teleseismic waveforms. (a) Vertical recordings are aligned by *P* arrivals on Global Seismographic Network (GSN) (black) and OBS stations (blue lines within the dashed box) with the GUMO and PA03 OBS station shown in red. (b) Vertical recordings on OBS stations. Only the polarity of PA03 OBS station is consistent with GUMO station, whereas other OBS stations are reversed. (c) Location of earthquake with focal mechanism, GSN stations (red triangles), and the OBS (yellow triangle). The color version of this figure is available only in the electronic edition.

reversed polarity, making any analysis based on ground motion in the tangential (T) and radial (R) directions difficult. Reversed polarities are common for seismic stations on land for a variety of reasons (Hurst *et al.*, 2002; Roman *et al.*, 2006; Sens-Schönfelder, 2008; Niu and Li, 2011; Yang *et al.*, 2012; Young *et al.*, 2016), even for some permanent stations (Ekström and Nettles, 2010; Li, Hauksson, and Andrews, 2019). Although it is straightforward to identify and correct reversed polarities for land stations using teleseismic waveforms, identifying and correcting polarities as well as orientations of OBS horizontal components are more difficult because they are coupled together.

We notice such problems of the OBS data at the southernmost Mariana subduction zone. The vertical components of a few OBSs are obviously flipped, as shown in the waveform records of one teleseismic earthquake on land stations in the similar azimuthal range (Fig. 1). However, without knowing whether the horizontal components suffer the same problem, we cannot correct their orientation using traditional methods. Unfortunately, because some of these OBS instruments were lost at sea or broken during other experiments shortly after the Mariana expedition, it is impossible for us to conduct laboratory consistency tests. Therefore, it is vital to estimate the orientation of OBS horizontal components with randomly flipping polarities. The results of OBS orientations are useful for conducting waveform-based seismic studies, such as earthquake focal mechanisms, which could facilitate the investigation of regional stress fields (Reyners *et al.*, 1997; Webb and Anderson, 1998; Evanzia *et al.*, 2017; Bloch *et al.*, 2018), the width of seismogenic zone on the megathrust (Emry *et al.*, 2011), and the depth extent of different types of faulting in the outer-rise region (Craig *et al.*, 2014; Emry *et al.*, 2014; Zhang *et al.*, 2014, 2018; Zhou *et al.*, 2015; Zhou and Lin, 2018).

In this study, we present a framework to correct orientations for OBSs with flipped waveforms. We first conduct a series of tests by artificially flipping polarity of the data recorded at Global Seismographic Network (GSN) stations, the horizontal orientations of which are already known to determine the influences of one or two reversed channels on orientation estimates based on polarization analysis. We then estimate orientations of the Mariana OBS horizontal components via analyzing polarization of teleseismic *P* waves and Rayleigh waves, as well as waveform modeling. Comparing the observed waveforms to synthetic waveforms could effectively solve the ambiguity of R and T directions caused by flipping polarity of OBS data. The results here could provide detailed specifications to correct orientations of OBSs or land stations with random polarity reversal. Such studies could also motivate efforts to develop and improve the manufacture of OBSs, as well as preparation of OBS data acquisition, for example, consistency testing of OBSs, prior to deployment.

Data Set and OBS Clock Error

The data analyzed in this article were collected during two OBS experiments in the southern Mariana subduction zone, including a total of 12 broadband OBSs, each of which was equipped with a three-component broadband seismograph and a hydrophone. During the first OBS experiment of "Challenger Deep" expeditions in December 2016, both active and passive source seismic experiments were carried out. The

active source seismic experiment lasted two weeks starting 1 December 2016 with 18 OBSs, based on which a 2D crustal *P*-wave velocity model was obtained (Wan *et al.*, 2019). For the passive source OBS experiment, seven long-term broadband OBSs were deployed in the fore-arc region, and six of them were recovered in June 2017 (the PA* OBS stations in Fig. 2) (Zhu *et al.*, 2019). Both the deployment and recovery of OBS instruments were conducted by R/V *Shiyan 3* of the South China Sea Institute of Oceanology, Chinese Academy of Sciences (CAS). The other six broadband OBS instruments (the PG* OBS stations in Fig. 2) were deployed by R/V *Tansuo 1* of the Institute of Deep-sea Science and Engineering, CAS, in March 2017 and recovered in June 2017 by R/V *Shiyan 3*; these instruments mostly cover the outer-rise region (Fig. 2).

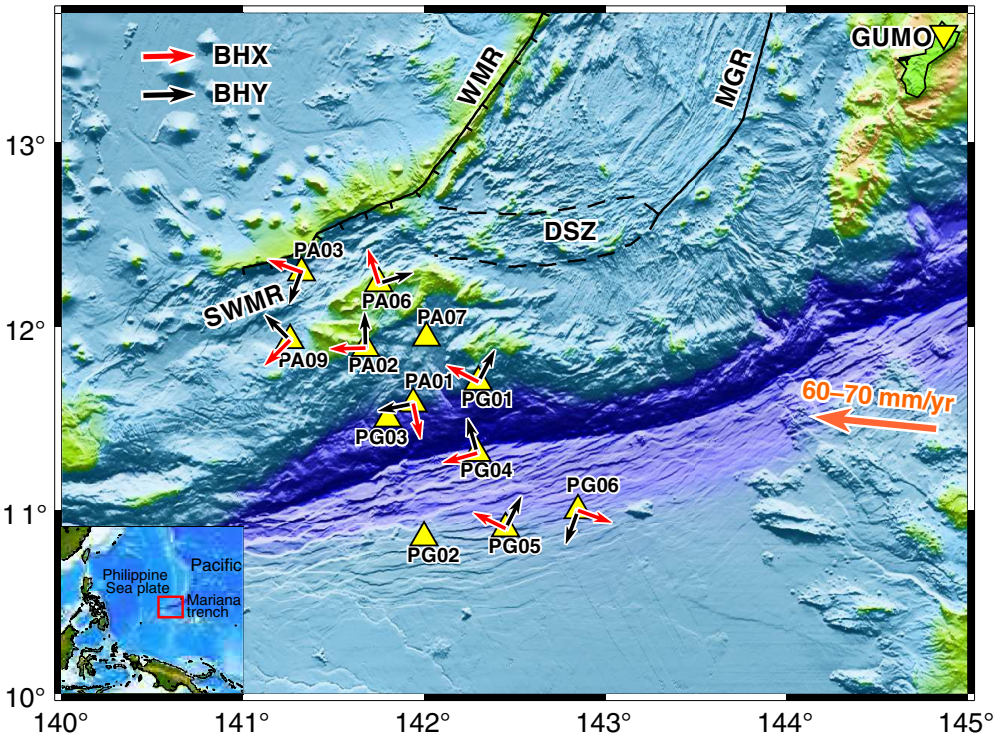

Figure 2. A map of OBS (yellow triangles) locations in the southern Mariana. Red and black arrows indicate the estimated orientations of BHX and BHY components, respectively. (Inset) Location of the study area (red frame). DSZ, diffuse spreading zone (Martinez *et al.*, 2018); MGR, Malaguana–Gadao ridges; SWMR, Southwest Mariana rift; WMR, West Mariana ridge. The color version of this figure is available only in the electronic edition.

We have inspected timing problems and corrected drifting for the PA* OBSs based on teleseismic differential travel times and ambient-noise cross correlation (Zhu *et al.*, 2019). Here, we followed the same procedure to check and correct the time errors for the PG* OBS stations. We found that all PG* OBS stations had negligible time drifting except the PG01 station, the time base of which sharply changed tens of seconds for many times during the deployment. Because of the temporal resolution of time symmetry analysis using noise cross-correlation functions, sharp changes within a short time period are hard to identify. Therefore, to inspect the detailed timing instability of PG01 station, we compared its observed and predicted travel times using available travel-time data of distant and local earthquakes.

For the distant earthquakes during the observed period, *P*-wave travel times at PG01 station deviated significantly from the predictions and observations at other OBSs. Furthermore, the differences changed with time, indicating variant timing errors during the deployment (Fig. 3). Because of the lack of moderate-size, distant earthquakes during the PG01 deployment, we checked the *P*-wave travel-time differences between observations and predictions of located local earthquakes (Zhu *et al.*, 2019), which show complicated changes in the PG01 station time base (Fig. 4). Despite the irregular time intervals between sudden jumps, the magnitude of each jump seems to be multiples of ~17.5 s.

To figure out the possible cause, we checked the raw data segments. According to the GPS synchronization recordings before deployment and after recovery, internal clock time error of PG01 station was only 0.08 s during the entire period, indicating that the reference time of each raw segment should be correct. However, the time lengths of segments with identical data points may abruptly change by multiples of ~17.5 s (Fig. 4), which is the reason for sudden jumps of observed *P*-wave travel time. What is more complicated is that *P*-wave travel-time differences between observations and predictions of local earthquakes shifted during the time span of one single segment, suggesting problems of the timing of internal sampling. During our process of correcting the orientations, we then applied different time shifts to account for the timing problem of the PG01 station for different time periods.

Polarity Reversal and Horizontal Orientation

The reversed vertical polarities of 11 OBS stations were identified according to teleseismic recordings compared with that at the adjacent GUMO and other GSN stations (Fig. 1). To check the stability of OBS polarity, we selected earthquakes

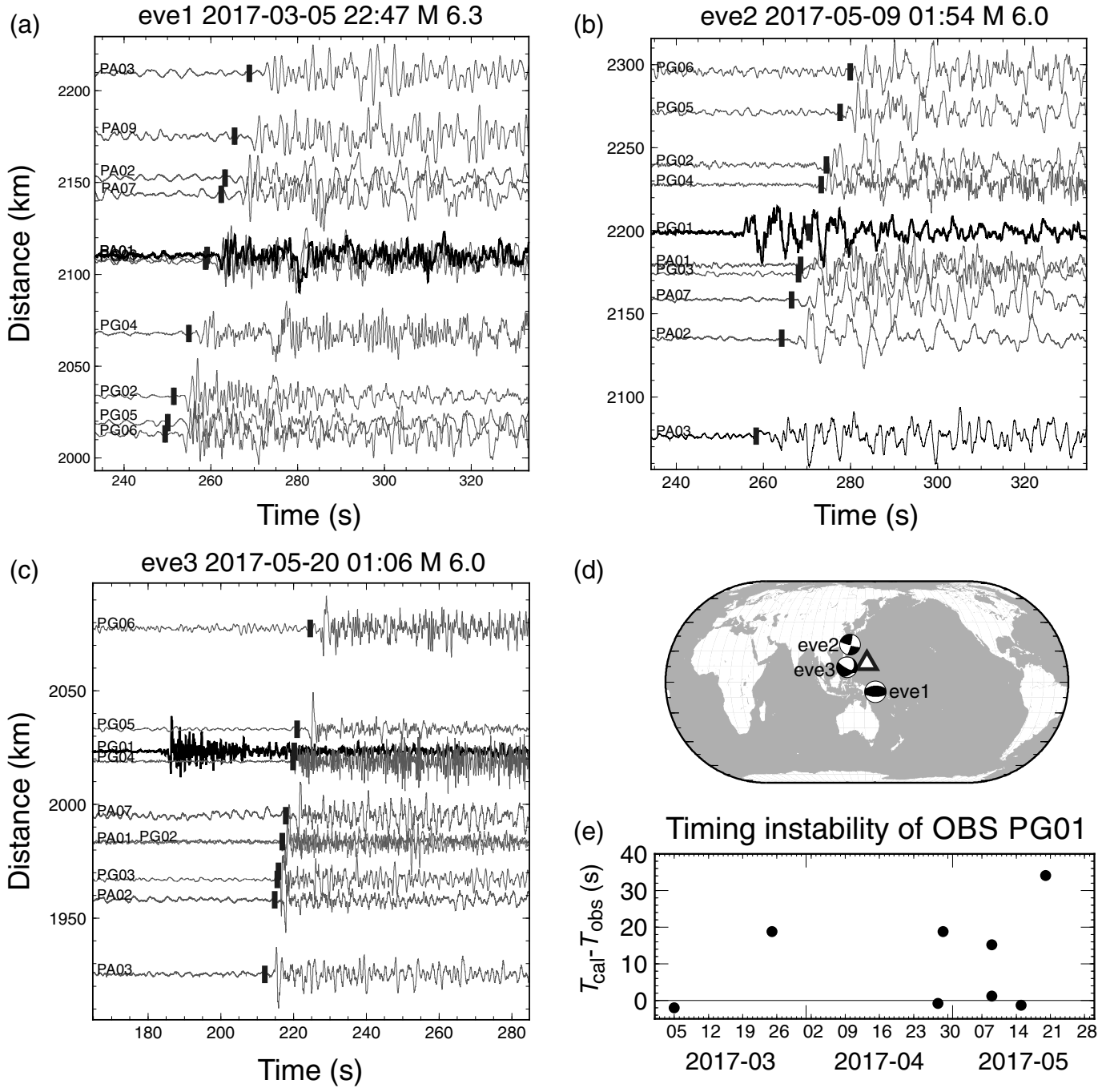

with different origin time, azimuth, and known Global Centroid Moment Tensor (Global CMT) solutions. After inspecting waveforms of earthquakes with clear *P* arrivals, we found that the vertical polarities of OBS stations remained reversed during the entire deployment. Such polarity reversal does not affect earthquake detection or location but inevitably influences the estimates of horizontal orientations.

Although we could directly correct the polarity of vertical components, it is much more challenging to use the same approach for horizontal components, because polarities are coupled with the unknown horizontal orientation. Furthermore, we did not know whether one or two horizontal

Figure 3. Timing instability of PG01 OBS station based on teleseismic waveforms. (a–c) Vertical OBS recordings of three earthquakes, focal mechanisms of which are shown in (d). Black bars indicate theoretical travel times of *P* waves based on the IASP91 velocity model. The PG01 has obvious timing changes. (d) A map showing distribution of the three earthquakes that occurred during the deployment of OBS (open triangle). (e) Time differences between the observed and theoretical arrivals of OBS PG01 station based on eight teleseismic earthquakes during the deployment.

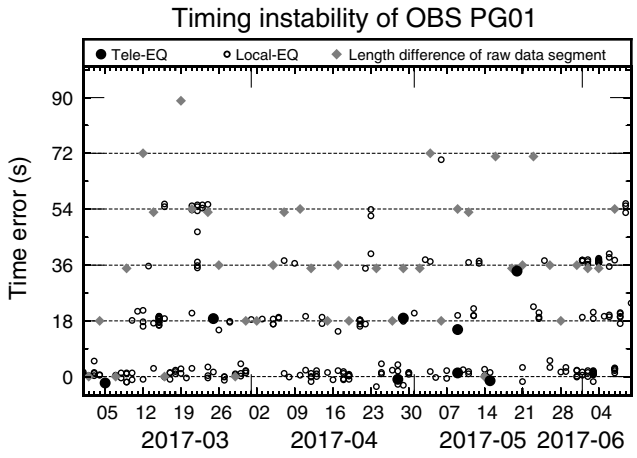

Figure 4. Time differences between the observed and theoretical arrivals of OBS PG01 station based on eight teleseismic earthquakes (black dots) and local earthquakes (open dots). Gray diamonds show the length differences of raw data segments relative to normal length. EQ, earthquake.

components of the OBSs were flipped. To tackle the challenge, we first conducted tests using the data of GSN stations to verify the influences from polarity reversal on estimating orientations based on methods of *P*-wave and Rayleigh-wave polarization. We then applied them to the OBS data and corrected the orientation and waveform polarity by waveform modeling.

Polarization analyses

Polarity reversal effects on orienting OBSs using Rayleigh-wave polarization. Azimuth can be determined via polarization analysis of the Rayleigh wave recorded on three-component sensors, as the Rayleigh wave exhibits retrograde elliptical particle motion in the vertical–radial plane (Laske, 1995; Baker and Stevens, 2004; Stachnik *et al.*, 2012; Scholz *et al.*, 2016). The polarization analysis is performed by cross correlating the vertical component with the Hilbert-transformed radial component. The 90° phase shift associated with the Hilbert transform yields a theoretically linear relation between the two signals (Baker and Stevens, 2004; Stachnik *et al.*, 2012; Zha *et al.*, 2013). For a sensor with unknown orientation, a grid search with 1° step in the 0°–359° range is conducted to find the optimal azimuth for which the normalized correlation coefficient of the vertical signal and Hilbert-transformed radial signal is a maximum.

To figure out the exact effects of polarity reversals on estimates of OBS horizontal orientations using polarization analysis of Rayleigh waves, we conducted a series of tests using teleseismic waveforms on land GSN stations the horizontal orientations of which are already known (Fig. 5). Seismograms of earthquakes with magnitude > 5.0, depth < 300 km, and the epicentral distance larger than 300 km were selected. Assuming the group velocity of a Rayleigh wave is 2.7–4.7 km/s, the time

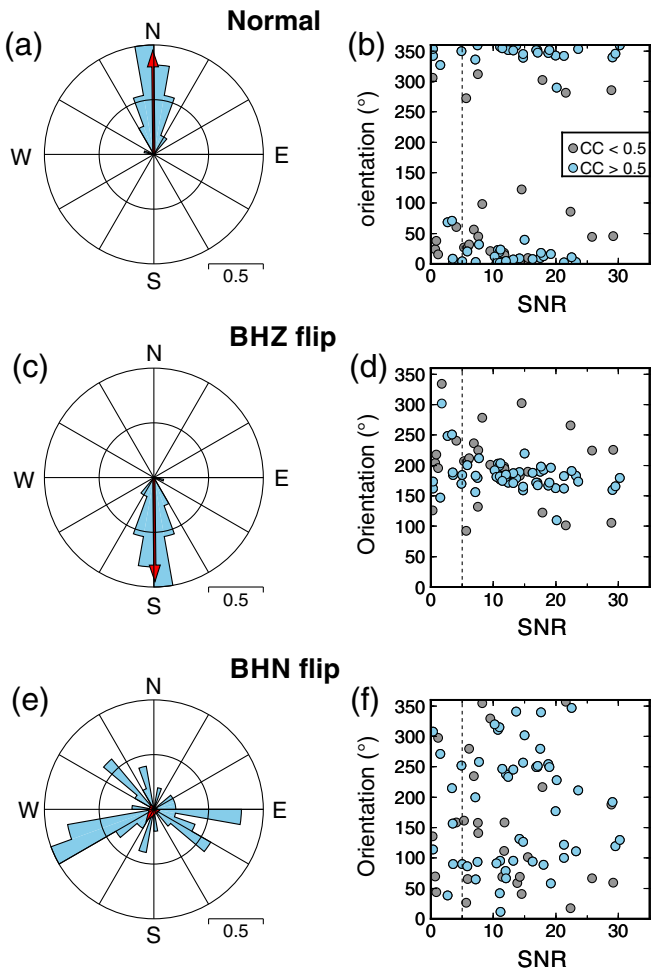

Figure 5. Testing the effects of polarity reversal on the estimated orientations using GUMO station. (a) Normalized polar distribution of estimated BHN orientations via polarization analysis of Rayleigh waves, with the normalized correlation coefficient (CC) > 0.5 and signal-to-noise ratio (SNR) > 5. The red arrow marks the mean value of estimated BHN orientations (358.8°). (b) Distribution of all estimated BHN orientations versus SNR, with blue dots (CC > 0.5) and gray dots (CC < 0.5). The vertical black dashed line marks the cutoff SNR value of 5. (c,d) The distribution of estimated BHN orientations with a flipped vertical component (BHZ). (e,f) The distribution of estimated BHN orientations with one flipped horizontal component (BHN).

window used for analysis is [distance/4.7 + 20 s, distance/2.7 s]. Different band-pass filters, 0.02–0.04 Hz, 0.03–0.05 Hz, and 0.04–0.06 Hz, were used (Baker and Stevens, 2004; Stachnik *et al.*, 2012). The estimates were well consistent for different filters. We then adopted two criteria to refine the estimates: (1) the SNR of the Rayleigh wave was larger than 5 on at least one horizontal component; Here, SNR was measured as a ratio of the energy within the selected time window to the energy of tailing noise. (2) The normalized correlation coefficient was larger than 0.5.

Under normal circumstances, estimated azimuth of BHN component is convergent toward north (Fig. 5a,b). When the vertical component is reversed, estimated azimuth of BHN component is (falsely) convergent toward south, but the estimates of azimuthal values are still focused (Fig. 5c,d). The wrong estimation caused by the vertical-component polarity reversal leads to reversed R and T components (Fig. 6a). In comparison, the estimates of the BHN component are highly scattered when only one horizontal component is reversed (Fig. 5e,f). The wrong estimation results in reversed T component (Fig. 6b). If two horizontal components are both reversed, the situation is the same with only a vertical polarity reversal.

Polarity reversal effects on orienting OBSs using *P*-wave polarization. We have also analyzed the polarization of the *P* wave based on the eigenvalue analysis (Flinn, 1965; D'Alessandro *et al.*, 2013). The procedure follows that of D'Alessandro *et al.* (2013) and is briefly described later. The three eigenvectors $\boldsymbol{v}_j (j = 1, 2, 3)$ with corresponding eigenvalues $\lambda_i (i = 1, 2, 3, \lambda_1 > \lambda_2 > \lambda_3)$, define the polarization ellipsoid of *P* waves. The level of linear polarization could be quantified by the linearity index, which varies from 0 to 1 (Fig. 7; D'Alessandro *et al.*, 2013):

$$\text{Linearity} = 1 - \left(\frac{\lambda_2 + \lambda_3}{2\lambda_1}\right). \quad (1)$$

Using the first *P* phase with high linearity, the back azimuth (baz_cal) can be computed by the following equation:

$$\text{baz}_{\text{cal}} = \arctan\left(\frac{\alpha_{21}}{\alpha_{31}}\right) + 180°, \quad (2)$$

in which α_{21} and α_{31} are the cosines of the angles between the eigenvector v_1 and the north–south and east–west directions, respectively. For a sensor (bhx) with unknown orientation (θ), the sensor orientation can be determined as:

$$\theta = \text{baz} - \text{baz}_{\text{cal}}, \quad (3)$$

in which baz is the station-to-event back azimuth along the great circle path and baz_cal is the estimated back azimuth.

We also tested the polarity reversal effects on orienting OBSs based on *P*-wave polarization using the GSN stations. Earthquakes in the epicentral distance greater than 300 km with **M** > 5.0 and clear *P* waves were selected. The time window of the initial *P* phase was manually selected for each earthquake (Fig. 7). Two criteria were adopted to refine the calculations: (1) SNR of the initial *P* wave should be larger than 5 on both horizontal components. Here, SNR was measured as the ratio of the energy within the selected initial *P*-wave window to the energy of heading noise; and (2) the linearity should be larger than 0.95.

The polarity reversal effects on *P*-wave polarization analysis are similar to that of Rayleigh-wave polarization. To summarize the effects, (1) a vertical flip leads to reversed but convergent estimations, resulting in reversed radial and tangential components; (2) one flipped horizontal component leads to false and nonconvergent orientations; and (3) the effects of two flipped horizontal components are the same as those of only the vertical polarity reversed.

Determination of orientation via synthetic waveforms

Although we can identify whether one horizontal component flipped based on the nonconvergent distribution of estimates of azimuthal values, we cannot distinguish between two flipped or two normal horizontal components because of the 180° ambiguity of R and T components. Therefore, we computed synthetic waveforms and conducted waveform modeling to solve the 180° ambiguity problem. If the observed R and T components are consistent with synthetics, the tentatively estimated optimal orientations are true and the polarities of horizontal components are normal. Otherwise, the estimated orientations will differ from the true values by 180°, and the two horizontal components are flipped.

The estimates of horizontal orientation were convergent for all OBS stations in the southern Mariana, indicating that their two horizontal components were either normal or reversed simultaneously. The tentatively optimal orientations were calculated as the circular mean of all acceptable measurements from both Rayleigh- and *P*-wave polarization, even though the number of Rayleigh-wave polarization measurements is usually larger than that of *P* waves due to higher signal amplitudes of Rayleigh waves. A bootstrap algorithm was adopted to estimate the 95% confidence interval of the mean orientation angle (Menke and Menke, 2009). The observed waveforms were first rotated to R and T directions according to the tentatively estimated orientations (but they may be wrong by 180° if the data were flipped).

To solve such ambiguity, we selected an M_w 6.8 earthquake (Table 1) and compared the synthetic waveforms to the observed tangential and radial seismograms on OBS stations. We adopted the frequency–wavenumber integration method (Zhu and Rivera, 2002) to compute Green's functions using the 1D IASP91 velocity model (Kennett and Engdahl, 1991). To validate our synthetics, we first compared them to observed seismograms on GSN stations (30°–90°). To improve fitting of *P* phases with observations, we slightly modified the source parameters of Global CMT solutions (Table 1) and then used the modified Global CMT solution (depth, magnitude, strike, dip, rake, and source duration) to compute synthetic waveforms (in velocity) (Fig. 8a). For the observed seismograms, the instrumental responses were removed, and the three-component seismograms were rotated to vertical, radial, and tangential components. We carefully selected traces by visual inspection and retained traces with clear *P* waves and *SH* waves. A 0.01–0.05 Hz band-pass

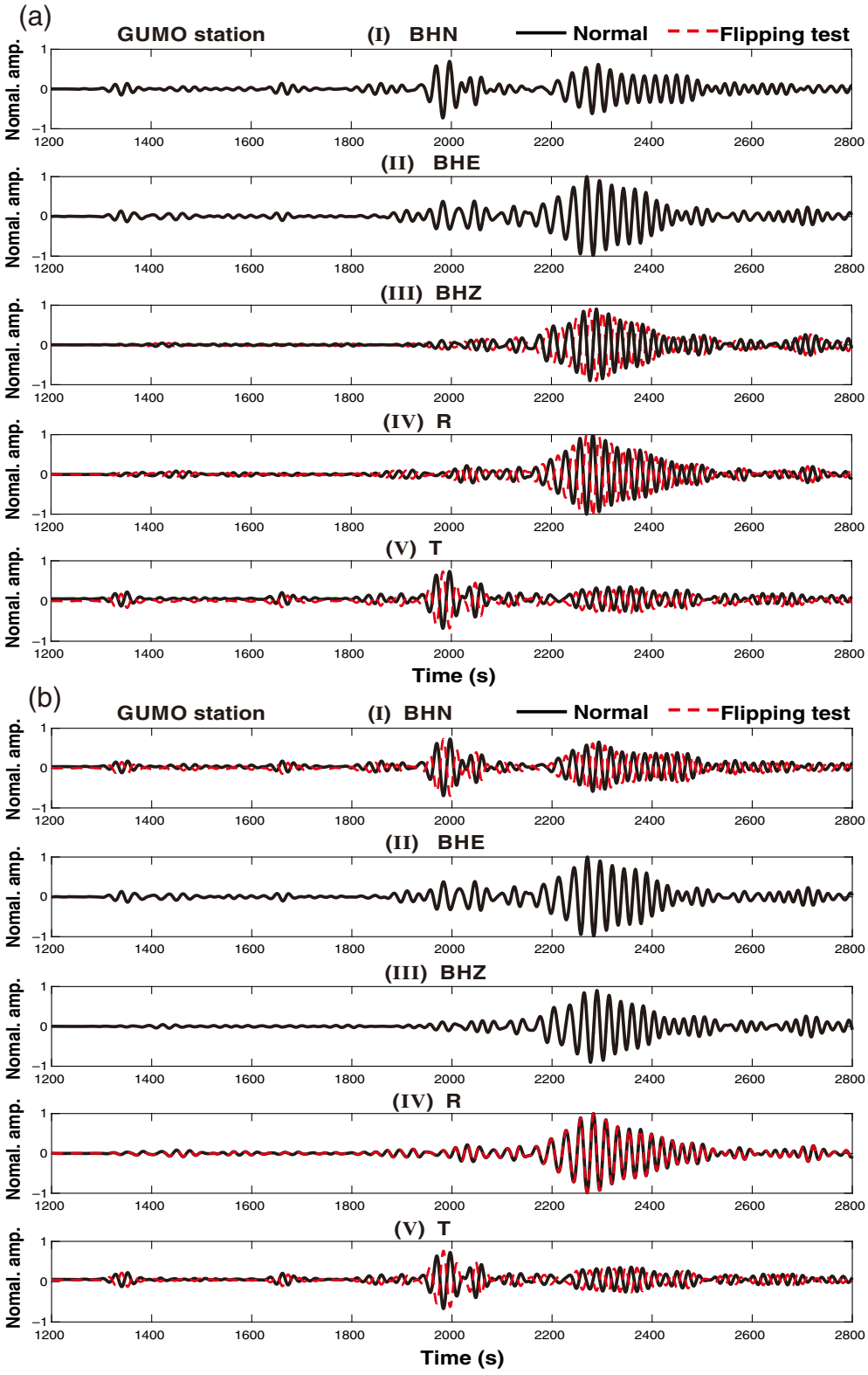

Figure 6. Testing effects of polarity reversal on orienting radial (R) and tangential (T) components using the GUMO station. Effects of (a) vertical polarity reversal and (b) one horizontal polarity reversal on analysis of Rayleigh-wave polarization and oriented R and T components. Information of the earthquake: original time 8 December 2016 14:49:45, latitude = 40.4535°, longitude = −126.1936°, event depth = 8.5 km. The color version of this figure is available only in the electronic edition.

filter was used for both synthetics and observations, which is slightly higher than that used for Global CMT solutions (~0.003–0.02 Hz; Ekström *et al.*, 2012). The different band-pass filters may slightly affect the choice of best-fitting source parameters.

We then compared synthetics to observations on OBS stations (Fig. 8b). Using the tentative orientation for each OBS, only the waveforms of PA03 were consistent with the synthetics. The observed R and T components of other OBSs were all flipped compared with the synthetics, demonstrating that their horizontal components were flipped simultaneously. After we corrected the flipped data, the polarities of observed waveforms were consistent with that of the GUMO station, as well as the synthetics on all three components (Fig. 8b). Therefore, we corrected the tentative horizontal orientation by 180° except for the PA03 station. After consultation with the manufacturer, we think that improper production process, such as erroneous cable wiring may be responsible for the flipped polarity of the OBS recordings at the southernmost Mariana subduction zone.

Because of the poor SNR on at least one component for three OBSs (PA07, PG02, and PG03), we could not determine their orientations, and thus obtained orientations for nine out of 12 OBSs. The estimated azimuth of horizontal BHX components for the nine OBSs were shown in Table 2 and Figure 2, based on which the observed waveforms were rotated to radial and tangential components (Fig. 8b).

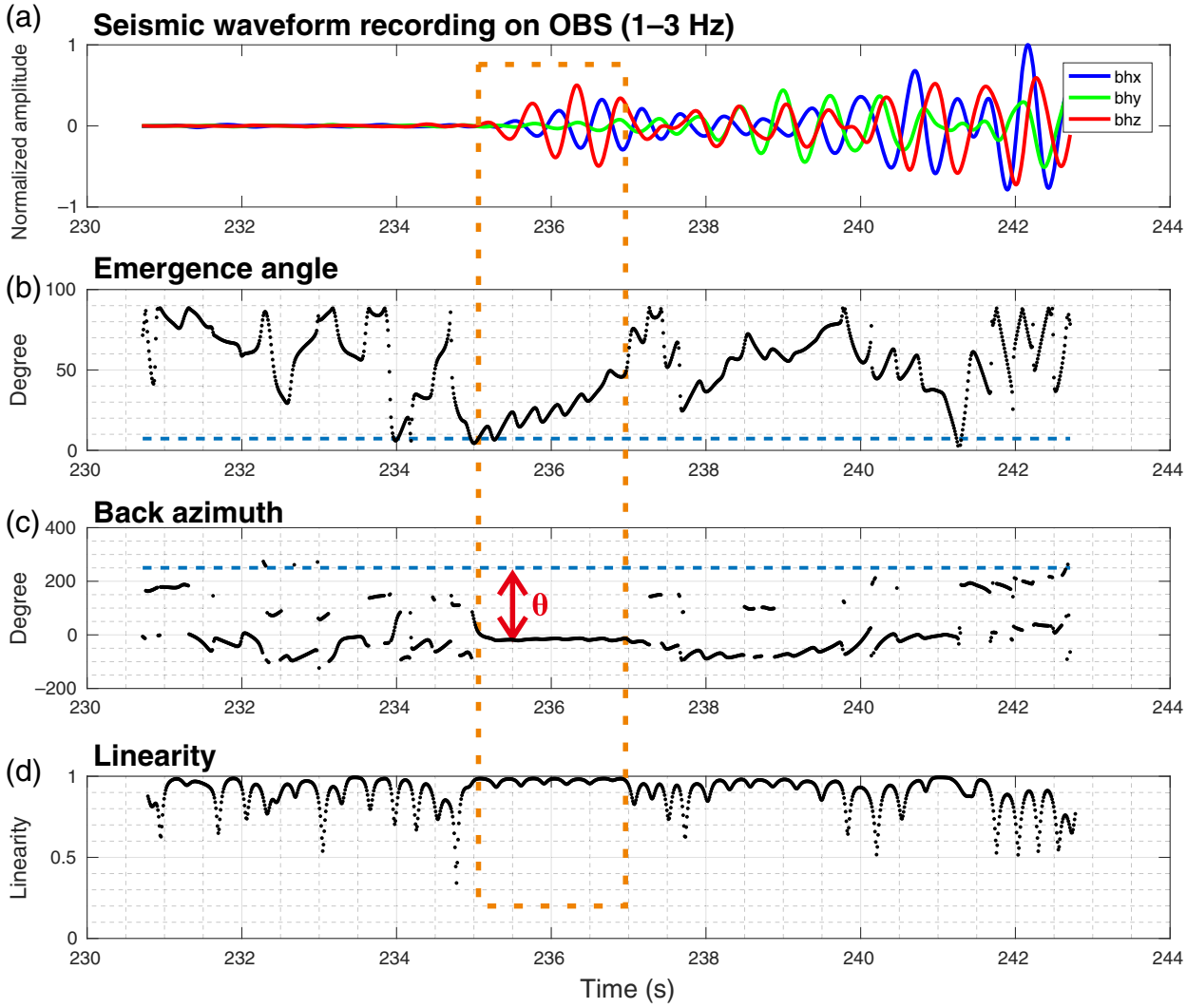

Discussion

It is necessary to correct horizontal orientations for OBS stations, which is vital for waveform-based seismic studies, such as earthquake focal mechanisms, anisotropy analysis (Katayama *et al.*, 2009), receiver functions (Hung *et al.*, 2019), and waveform tomography (Li *et al.*, 2007; Yang and Zhu, 2010; Sun and Helmberger, 2011). Although many traditional methods based on polarization analyses have been used to calculate horizontal orientations, these methods will get false orientations when an OBS suffers flipped polarities or mislabeling channels. The procedure presented in this study could

Figure 7. Time-domain polarization analysis of the *P* wave recorded by PA02 OBS station. The initial *P* phase with a good linearity index within the dashed golden box is used to estimate the back azimuth. (a) The three-component seismograms with a 1–3 Hz band-pass filter. (b) The comparison of calculated emergence angles between polarization analysis (black dots) and geometric methods (dashed blue line). (c) The estimated back azimuth by polarization analysis (black dots) and geometric methods (dashed blue line). The average value within the dashed box is regarded as the optimal back azimuth. (d) The linearity index of seismic waves. The color version of this figure is available only in the electronic edition.

TABLE 1
Global Centroid Moment Tensor (Global CMT) Solution and Modified Source Parameters of the M_w 6.8 Earthquake at 9 May 2017 13:52

Sources	Latitude (°)	Longitude (°)	Depth (km)	Strike (°)	Dip (°)	Slip (°)	M_w	Duration (s)
Global CMT	−14.55	167.20	181.4	177	49	125	6.8	5.9
This study	−14.55	167.20	**170.0**	177	**42**	125	6.8	**3.0**

Bold values are the modified parameters different from the Global CMT values.

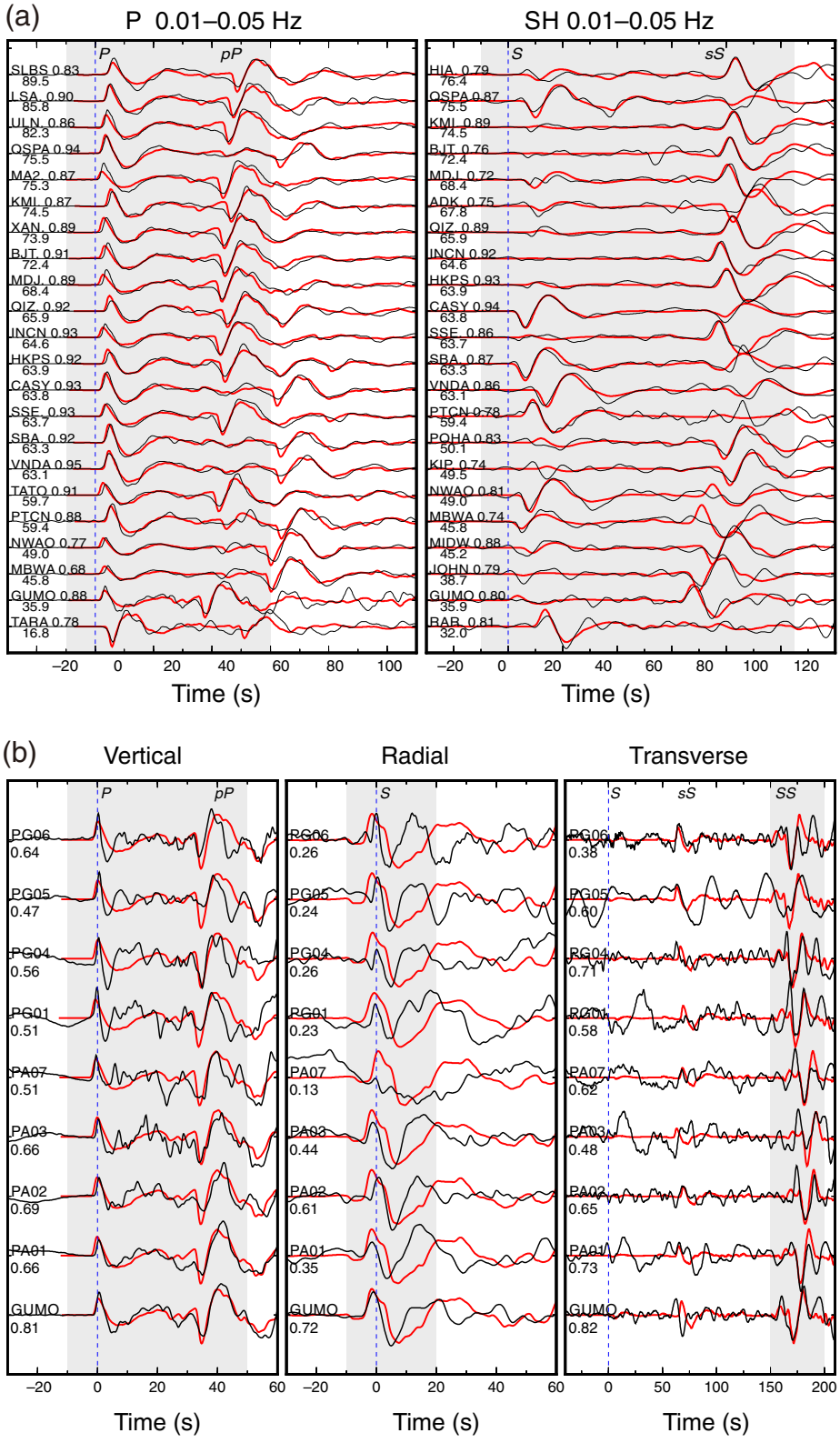

Figure 8. Comparison between the observed (black lines) and synthetic (red lines) waveforms of an M_w 6.8 event. The synthetics are calculated based on modified Global Centroid Moment Tensor (Global CMT) solution (Table 1). (a) The GSN stations. The number behind the station name shows the cross-correlation coefficient of waveforms in the light gray window. The number below the station name marks the epicentral distance in degrees. (b) The OBS stations. The number below the station name shows the cross-correlation coefficient of waveforms in the light gray shadow. The color version of this figure is available only in the electronic edition.

effectively distinguish one from two flipped horizontal components and eliminate the 180° ambiguity caused by flipped polarity, taking advantage of channel-to-channel comparison between observed and synthetic waveforms. One obvious advantage of the procedure is that the flipped channels could be identified and corrected without the need for laboratory tests. Of course, it requires clear OBS waveforms from at least one teleseismic event. Although the waveform fittings on the R and T components are not as good as those on the vertical components due to the typically low SNR of horizontal components, the oriented waveforms from the southern Mariana OBS array are highly consistent with waveforms from the nearby GUMO station, indicating robust orientation measurements. Therefore, it is also practical to cross correlate the OBS recordings with waveforms of well-oriented land stations, if teleseismic waveforms are too noisy.

Large noise level on the R and T components can be caused by a variety of factors, including coupling condition, local currents, and other uncorrelated noises (Trehu, 1985; Webb, 1998; Lin *et al.*, 2010; Webb and Crawford, 2010). Previous studies have indicated constantly changing noise level or coupling condition between OBS and seafloor (Trehu, 1985; Webb, 1998; Webb and Crawford, 2010). Such noise will affect inversion of earthquake focal mechanisms, which rely heavily on the ground motion caused only by seismic signals. Therefore, to calculate the earthquake focal mechanisms,

TABLE 2
Estimated Orientation of Horizontal BHX Components and Polarities of Vertical Components

Components	PA01	PA02	PA03	PA06	PA09	PG01	PG04	PG05	PG06
BHX mean ± 95% CI (°)	168.3 ± 13.6	268.6 ± 11.8	290.3 ± 8.1	342.4 ± 6.5	225.2 ± 8.8	297.1 ± 7.2	254.1 ± 9.4	296.1 ± 10.4	109.9 ± 10.8
BHZ polarity	−1	−1	1	−1	−1	−1	−1	−1	−1

CI, confidence interval.

systematic calibrations of ground motion for each OBS should be addressed in future studies.

In addition to diagnosing the polarity and horizontal orientation of OBSs, the procedure presented in this study may also be useful to correct land seismic stations. Ekström and Nettles (2010) report the erratic behavior of the horizontal components of some GSN stations due to chronic sensor problems. Niu and Li (2011) suggest that about one-third of the China Digital Seismic Network stations have problems, including misorientation of the two horizontal components, mislabeling, and polarity reversal in one or more components. Li, Hauksson, and Andrews (2019), Li, Hauksson, Heaton, *et al.* (2019) find that four permanent stations of Southern California Seismic Network (SCSN) were flipped in horizontal directions and about 5% of stations of the SCSN have data issues to various extents (Li, Hauksson, and Andrews, 2019; Li, Hauksson, Heaton, *et al.*, 2019). When a retroactive remedy for these problems is impossible, we could diagnose the problems following the analysis in this study.

Conclusions

We have presented detailed approaches to orient OBS horizontal components with polarity reversals and solve the ambiguity of radial and tangential directions via waveform modeling. Orientation results of the southern Mariana OBS array produce waveforms that are highly consistent with waveforms of the on-land GUMO station, indicating that the approaches provide robust retrieval of horizontal OBS signals. The effects of flipping polarity on polarization analysis have been tested using GSN stations: (1) a vertical component flip leads to reversed but convergent estimations, resulting in reversed radial and tangential components; (2) one horizontal-component flip leads to false and nonconvergent estimates on orientations; and (3) the effect of two flipped horizontal components is the same as a flipped vertical component.

Data and Resources

We collected the seismograms of Global Seismographic Network (GSN) stations via the Incorporated Research Institutions for Seismology (IRIS). The Global Centroid Moment Tensor (Global CMT) Project database was searched using www.globalcmt.org/CMTsearch.html. Seismic Analysis Code (SAC), MATLAB, and TauP Toolkit (Crotwell *et al.*, 1999) were used in our study. Software packages Generic Mapping Tools (Wessel and Smith, 1991) and PSSAC (developed by Lupei Zhu) were used for data analysis and figure preparation in this study.

Acknowledgments

The authors are grateful to Associate Editor Zefeng Li and one anonymous reviewer for their constructive comments that improved this article. Thanks to the science parties and crew members of the R/V *Shiyan 3* and *Tansuo 1* for deployment and collection of the ocean-bottom seismometer (OBS) instruments. This study is supported by the Hong Kong Research Grant Council Grants (Number 14313816), Faculty of Science at the Chinese University of Hong Kong (CUHK), Chinese Academy of Sciences (CAS; Numbers Y4SL021001, QYZDY-SSW-DQC005, 133244KYSB20180029, and XDB06030201), the National Natural Science Foundation of China (Numbers 41890813, 91628301, 91858207, and U1606401), the National Key R&D Program of China (2018YFC0309800 and 2018YFC0310100), and Southern Marine Science and Engineering Guangdong Laboratory (Guangzhou) (GML2019ZD0205).

References

Baker, G. E., and J. L. Stevens (2004). Backazimuth estimation reliability using surface wave polarization, *Geophys. Res. Lett.* **31,** L09611, doi: 10.1029/2004GL019510.

Barklage, M., D. A. Wiens, J. A. Conder, S. Pozgay, H. Shiobara, and H. Sugioka (2015). P and S velocity tomography of the Mariana subduction system from a combined land-sea seismic deployment, *Geochem. Geophys. Geosys.* **16,** 3, 681–704.

Bloch, W., B. Schurr, J. Kummerow, P. Salazar, and S. A. Shapiro (2018). From slab coupling to slab pull: Stress segmentation in the subducting Nazca Plate, *Geophys. Res. Lett.* **45,** 5407–5416.

Cai, C., D. A. Wiens, W. Shen, and M. Eimer (2018). Water input into the Mariana subduction zone estimated from ocean-bottom seismic data, *Nature* **563,** 389–392.

Craig, T. J., A. Copley, and J. Jackson (2014). A reassessment of outer-rise seismicity and its implications for the mechanics of oceanic lithosphere, *Geophys. J. Int.* **197,** 63–89.

Crawford, W. C., and S. C. Webb (2000). Identifying and removing tilt noise from low-frequency (0.1 Hz) seafloor vertical seismic data, *Bull. Seismol. Soc. Am.* **90,** 952–963.

Crotwell, H. P., T. J. Owens, and J. Ritsema (1999). The TauP toolkit: Flexible seismic travel-time and ray-path utilities, *Seismol. Res. Lett.* **70,** 154–160.

D'Alessandro, A., G. Mangano, G. D'Anna, and D. Luzio (2013). Waveforms clustering and single-station location of microearthquake multiplets recorded in the northern Sicilian offshore region, *Geophys. J. Int.* **194,** 1789–1809.

Ekström, G., and M. Nettles (2010). Performance of the GSN station CASY-IU, 1996-2009, *Waveform Quality Center Rept. 2010:1*.

Ekström, G., M. Nettles, and A. M. Dziewoński (2012). The global CMT project 2004–2010: Centroid-moment tensors for 13,017 earthquakes, *Phys. Earth Planet. In.* **200/201,** 1–9.

Emry, E. L., D. A. Wiens, and G. C. Daniel (2014). Faulting within the Pacific plate at the Mariana trench: Implications for plate interface coupling and subduction of hydrous minerals, *J. Geophys. Res.* **119,** 3076–3095.

Emry, E. L., D. A. Wiens, H. Shiobara, and H. Sugioka (2011). Seismogenic characteristics of the Northern Mariana shallow thrust zone from local array data, *Geochem. Geophys. Geosys.* **12,** no. Q12008, doi: 10.1029/2011GC003853.

Evanzia, D., T. Wilson, M. K. Savage, S. Lamb, and H. Hirschberg (2017). Stress orientations in a locked subduction zone at the southern Hikurangi margin, New Zealand, *J. Geophys. Res.* **122,** 7895–7911.

Flinn, E. A. (1965). Signal analysis using rectilinearity and direction of particle motion, *Proc. IEEE* **53,** 1874–1876.

Hung, T. D., T. Yang, B. M. Le, and Y. Yu (2019). Effects of failure of the ocean-bottom seismograph leveling system on receiver function analysis, *Seismol. Res. Lett.* **90,** 1191–1199.

Hurst, A. W., H. M. Bibby, and R. R. Robinson (2002). Earthquake focal mechanisms in the central Taupo Volcanic Zone and their relation to faulting and deformation, *New Zeal. J. Geol. Geophys.* **45,** 527–536.

Katayama, I., K.-i. Hirauchi, K. Michibayashi, and J.-i. Ando (2009). Trench-parallel anisotropy produced by serpentine deformation in the hydrated mantle wedge, *Nature* **461,** 1114.

Kennett, B. L. N., and E. R. Engdahl (1991). Travel times for global earthquake location and phase association, *Geophys. J. Int.* **105,** 429–465.

Laske, G. (1995). Global observation of off-great-circle propagation of long-period surface waves, *Geophys. J. Int.* **123,** 245–259.

Le, B. M., T. Yang, Y. J. Chen, and H. Yao (2018). Correction of OBS clock errors using Scholte waves retrieved from cross-correlating hydrophone recordings, *Geophys. J. Int.* **212,** 891–899.

Li, H., L. Zhu, and H. Yang (2007). High-resolution structures of the Landers fault zone inferred from aftershock waveform data, *Geophys. J. Int.* **171,** no. 3, 1295–1307.

Li, Z., E. Hauksson, and J. Andrews (2019). Methods for amplitude calibration and orientation discrepancy measurement: Comparing collocated sensors of different types in Southern California Seismic Network, *Bull. Seismol. Soc. Am.* **109,** no. 4, 1563–1570.

Li, Z., E. Hauksson, T. Heaton, L. Rivera, and J. Andrews (2019). Monitoring data quality by comparing collocated broadband and strong-motion waveforms in Southern California Seismic Network, *Seismol. Res. Lett.* **90,** no. 2A, 699–707.

Lin, C.-R., B.-Y. Kuo, W.-T. Liang, W.-C. Chi, Y.-C. Huang, C. John, and C.-Y. Wang (2010). Ambient noise and teleseismic signals recorded by ocean-bottom seismometers offshore eastern Taiwan, *Terr. Atmos. Ocean. Sci.* **21,** 743–755.

Martinez, F., R. J. Stern, K. A. Kelley, Y. Ohara, J. D. Sleeper, J. M. Ribeiro, and M. Brounce (2018). Diffuse extension of the southern Mariana margin, *J. Geophys. Res.* **123,** 892–916.

Menke, W., and J. Menke (2009). *Environmental Data Analysis with MATLAB*, Elsevier, New York, New York, 288 pp.

Niu, F., and J. Li (2011). Component azimuths of the CEArray stations estimated from P-wave particle motion, *Earthq. Sci.* **24,** 3–13.

Reyners, M., R. Robinson, and P. McGinty (1997). Plate coupling in the northern South Island and southernmost North Island, New Zealand, as illuminated by earthquake focal mechanisms, *J. Geophys. Res.* **102,** 15,197–15,210.

Roman, D. C., J. Neuberg, and R. R. Luckett (2006). Assessing the likelihood of volcanic eruption through analysis of volcanotectonic earthquake fault-plane solutions, *Earth Planet. Sci. Lett.* **248,** 244–252.

Rueda, J., and J. Mezcua (2015). Orientation analysis of the Spanish broadband national network using Rayleigh-wave polarization, *Seismol. Res. Lett.* **86,** 929–940.

Scholz, J.-R., G. Barruol, F. R. Fontaine, K. Sigloch, W. C. Crawford, and M. Deen (2016). Orienting ocean-bottom seismometers from *P*-wave and Rayleigh wave polarizations, *Geophys. J. Int.* **208,** 1277–1289.

Sens-Schönfelder, C. (2008). Synchronizing seismic networks with ambient noise, *Geophys. J. Int.* **174,** 966–970.

Stachnik, J. C., A. F. Sheehan, D. W. Zietlow, Z. Yang, J. Collins, and A. Ferris (2012). Determination of New Zealand ocean bottom seismometer orientation via Rayleigh-wave polarization, *Seismol. Res. Lett.* **83,** 704–713.

Sun, D., and D. Helmberger (2011). Upper-mantle structures beneath USArray derived from waveform complexity, *Geophys. J. Int.* **184,** 416–438.

Tibi, R., D. A. Wiens, and X. Yuan (2008). Seismic evidence for widespread serpentinized forearc mantle along the Mariana convergence margin, *Geophys. Res. Lett.* **35,** L13303, doi: 10.1029/2008GL034163.

Trehu, A. (1985). A note on the effect of bottom currents on an ocean bottom seismometer, *Bull. Seismol. Soc. Am.* **75,** 1195–1204.

Vidale, J. E. (1986). Complex polarization analysis of particle motion, *Bull. Seismol. Soc. Am.* **76,** 1393–1405.

Wan, K., J. Lin, S. Xia, J. Sun, M. Xu, H. Yang, Z. Zhou, X. Zeng, J. Cao, and H. Xu (2019). Deep seismic structure across the southernmost Mariana trench: Implications for arc rifting and plate hydration, *J. Geophys. Res.* **124,** 4710–4727.

Webb, S. C. (1998). Broadband seismology and noise under the ocean, *Rev. Geophys.* **36,** 105–142.

Webb, S. C., and W. C. Crawford (2010). Shallow-water broadband OBS seismology, *Bull. Seismol. Soc. Am.* **100,** 1770–1778.

Webb, T. H., and H. Anderson (1998). Focal mechanisms of large earthquakes in the North Island of New Zealand: Slip partitioning at an oblique active margin, *Geophys. J. Int.* **134,** 40–86.

Wessel, P., and W. H. F. Smith (1991). Free software helps map and display data, *Eos Trans. AGU* **72,** 441–446.

Xu, H., Y. Luo, C.-C. Tang, K. Zhao, J. Xie, and X. Yang (2018). Systemic comparison of seismometer horizontal orientations based on teleseismic earthquakes and ambient-noise data, *Bull. Seismol. Soc. Am.* **108,** no. 6, 3576–3589.

Yang, H., and L. Zhu (2010). Shallow low-velocity zone of the San Jacinto fault from local earthquake waveform modelling, *Geophys. J. Int.* **183,** 421–432.

Yang, W., E. Hauksson, and P. M. Shearer (2012). Computing a large refined catalog of focal mechanisms for southern California

(1981-2010): Temporal stability of the style of faulting, *Bull. Seismol. Soc. Am.* **102,** 1179–1194.

Young, B. A., K. C. Chen, B. S. Huang, and J. M. Chiu (2016). Identification and elimination of data peculiarities in the strong-motion downhole array in Taipei basin, *Seismol. Res. Lett.* **88,** 82–95.

Zha, Y., S. C. Webb, and W. Menke (2013). Determining the orientations of ocean bottom seismometers using ambient noise correlation, *Geophys. Res. Lett.* **40,** 3585–3590.

Zhang, F., J. Lin, and W. Zhan (2014). Variations in oceanic plate bending along the Mariana trench, *Earth Planet. Sci. Lett.* **401,** 206–214.

Zhang, F., J. Lin, Z. Zhou, H. Yang, and W. Zhan (2018). Intra- and intertrench variations in flexural bending of the Manila, Mariana and global trenches: Implications on plate weakening in controlling trench dynamics, *Geophys. J. Int.* **212,** 1429–1449.

Zhou, Z., and J. Lin (2018). Elasto-plastic deformation and plate weakening due to normal faulting in the subducting plate along the Mariana Trench, *Tectonophysics* **734/735,** 59–68.

Zhou, Z., J. Lin, M. D. Behn, and J. A. Olive (2015). Mechanism for normal faulting in the subducting plate at the Mariana Trench, *Geophys. Res. Lett.* **42,** 4309–4317.

Zhu, G., H. Yang, J. Lin, Z. Zhou, M. Xu, J. Sun, and K. Wan (2019). Along-strike variation in slab geometry at the southern Mariana subduction zone revealed by seismicity through ocean bottom seismic experiments, *Geophys. J. Int.* **218,** 2122–2135.

Zhu, L., and L. A. Rivera (2002). A note on the dynamic and static displacements from a point source in multilayered media, *Geophys. J. Int.* **148,** 619–627.

Manuscript received 28 August 2019
Published online 12 February 2020